


Convex Optimization-based Entry Guidance for Spaceplane

Juho Bae, Sang-Don Lee, Young-Won Kim, Chang-Hun Lee* , and Sung-Yug Kim

Abstract: This paper aims to propose convex-optimization-based entry guidance for a spaceplane, which has potential in online implementation with less sensitivity to initial guess accuracy while mitigating a high-frequency jittering issue in the entry trajectory optimization problem. To this end, a highly nonlinear, constrained, and non-convex entry guidance problem is converted into sequential convex sub-problems in the second-order cone programming (SOCP) form by an appropriate combination of successive linearization and convexification techniques. From the investigation on the potential sub-problem infeasibility due to a rough initial guess for radial distance, a linear penalized term associated with a virtual control for an inequality constraint is used to relieve the sub-problem infeasibility while preserving the standardized SOCP form. An adjustable trust-region bound is also adopted in the proposed approach to improve the convergence property further. Additionally, a change of control variables and a relaxation technique are utilized to relieve the high-frequency jittering issue. It is proven that the Lossless convexification property is preserved for the relaxed problem even in the presence of the penalty terms. The feasibility of the proposed method is investigated through numerical simulations.

Keywords: Convex optimization, entry guidance, second-order cone programming (SOCP), trajectory optimization.

1. INTRODUCTION

Over the past several decades, there has been profound attention to spaceplanes (types of reentry vehicles) for space tourism, space transportation, and space exploration [1]. It is recognized that entry guidance plays a vital role in reentry vehicles. The ultimate goal of the entry guidance is to produce steering commands to guide a reentry vehicle from an entry interface point (EIP) to a specified target point while satisfying various constraints and dissipating mechanical energy for safe recovery. As the entry guidance problem is characterized by numerous practical constraints, highly time-variant, and nonlinear dynamics [2,3], it has been considered a challenging problem in guidance technology. Previous studies on the entry guidance can be classified into three categories: variant of the Shuttle entry guidance, predictor-corrector method, and trajectory optimization approach.

The Shuttle entry guidance [4] has been devised for the Shuttle operations, and its performance has been successfully demonstrated through numerous flight tests [5]. The underlying concept of the Shuttle entry guidance is to set a reference drag acceleration profile satisfying flight con-

straints and to track the reference drag profile using a linear feedback control law [4]. In the last few decades, there have been several variants of the Shuttle entry guidance with the purpose of improving its performance. In [6], a new Shuttle entry guidance with an energy-dependent reference drag profile was proposed for more accurate guidance performance. In [7], a nonlinear control approach was applied to designing the feedback control law for the reference drag following. The author in [8] devised new entry guidance with the optimal reference drag profile and nonlinear trajectory control law. However, as the Shuttle entry guidance relies on the predetermined reference drag profile, onboard applications intended to cope with unexpected situations are limited.

Hence, the predictor-correct approach, which relies more on onboard computation for an entry trajectory and guidance command, has been investigated as an alternative way in recent years. The basic idea of this approach is to iteratively determine a complete profile for the bank angle magnitude while meeting boundary conditions through numerical integration [9]. Explicitly handling inequality constraints is limited in the general predictor-corrector approach, and this method is also vulnerable to

Manuscript received July 10, 2021; revised August 27, 2021; accepted September 30, 2021. Recommended by Associate Editor Jong-Han Kim under the direction of Editor Hyo-Sung Ahn. This work has been supported by the Korea Aerospace Research Institute (KARI)'s own research project titled "Base Technology for Flight Control of Gliding and Landing for Spaceplanes."

Juho Bae is with the Department of Electrical Engineering, Korea Advanced Institute Science and Technology (KAIST), Daehak-ro, Yuseong-gu, Daejeon 34141, Korea (e-mail: johnbae1901@kaist.ac.kr). Sang-Don Lee, Young-Won Kim, and Chang-Hun Lee are with the Department of Aerospace Engineering, Korea Advanced Institute Science and Technology (KAIST), 291 Daehak-ro, Yuseong-gu, Daejeon 34141, Korea (e-mails: {sedan96, foreverkim, lckdgn}@kaist.ac.kr). Sung-Yug Kim is with the UAV Research Department, Korea Aerospace Research Institute, Daejeon 34133, Korea (e-mail: kkisy@kari.re.kr).

* Corresponding author.

modeling error. For these reasons, some modifications of this method have been reported in recent years. In [10], new predictor-corrector entry guidance was devised to enforce the inequality constraints effectively by utilizing the quasi-equilibrium glide condition (QEGC). In [11], a fully constrained predictor-corrector entry guidance was suggested using a modified QEGC. In [12], a unified form of predictor-corrector guidance was suggested for various types of reentry vehicles. Although the previous studies on the predictor-corrector approach could show potential in onboard applications than the Shuttle entry guidance, this approach still has weak points. The optimality of entry trajectory cannot be addressed in this approach, and the computational complexity is still high to be implemented online.

More recently, as remedies, a trajectory optimization approach, based on the computational guidance and control philosophy [13,14], has been investigated according to the mathematical developments and the computational capability improvements. The key ingredient for this approach is the convex optimization technique: it allows to effectively solve optimization problems in a polynomial time. The convex optimization technique has recently been applied to various engineering problems [15–18], including guidance applications. In [19], the entry guidance problem was formulated in the form of second-order cone programming (SOCP) to leverage favorable features of the convex optimization technique, and it was solved by the successive convexification method [20,21]. In [22], a new entry guidance problem was formulated in the sequential convex optimization framework by introducing a new control input. In [23], successive convex programming for the online trajectory generation and tracking of the reference trajectory was devised. For a rapid entry trajectory generation, the pseudospectral method and an improved successive convexification were applied to an entry guidance problem [24]. The authors in [25] proposed two methods for improving the convergence characteristic of the sequential convex programming method: line-search and trust-region techniques. The authors in [26] developed a convex optimization-based approach for rapidly generating an aerocapture trajectory. In [27], entry guidance considering no-fly-zone constraints was developed based on multiphase convex programming.

As the equations of motion for the entry guidance problem are highly nonlinear in general, sequential convex programming (SCP) with the successive linearization technique [20] has been widely adopted in previous studies. In the generic SCP method, a nonlinear optimization problem is sequentially solved by converting it into a convex sub-problem at each iteration. Although a strict convergence property of the convex optimization is weakened in the SCP method, it still has been recognized as an efficient heuristic method for solving nonlinear optimization problems. Moreover, it has been successfully applied to a

real-world guidance problem [28]. However, there are still some issues to be improved in the generic SCP method in the entry trajectory optimization problem.

First, the sub-problem infeasibility issue due to a poor initial guess of a solution is considered as an obstacle for the generic SCP method. To be more specific, in the successive linearization process, as a nonlinear optimization problem is convexified in the neighborhood of initial guess in early iterations, the convex sub-problem could be infeasible when an initial guess is too inaccurate. If the sub-problem infeasibility occurs, the successive convexification process no longer proceeds, and the convergence is failed. Accordingly, some studies handling this issue have been reported in the open literature recently. In [29], a dynamic relaxation term, which is regarded as a virtual control, was introduced to prevent the artificial infeasibility caused by the successive convexification sequence with a poor initial guess. The authors in [30] suggested a penalized SCP method by utilizing a linear penalty term in standard optimization [31]. Two pairs of positive slack variables were introduced to inequality constraints and equality constraints, respectively, and the linear penalty term with these slack variables was augmented into the performance index. In [24], a combination of L_1 and L_2 penalty terms was suggested to relieve the convex sub-problem infeasibility. Indeed, the occurrence of sub-problem infeasibility is closely related to the underlying nature of a given problem and a way of initial guess. Thus, only necessary relaxation terms should be introduced to a given problem. However, this point was less addressed in the previous studies.

When applying the SCP method to the entry trajectory optimization problem, another issue is a high-frequency jittering observed in the control profile, as reported in [19,22]. A similar issue has been reported when the entry trajectory optimization problem is solved by an NLP (nonlinear programming) solver, especially a sequential quadratic programming method in [32,33]. The main reason for the jittering is the dynamic coupling of state and control variables in the entry trajectory optimization problem. Thus, the key to suppressing the undesirable jittering in the control profile is to convert the coupled dynamics into dynamics in the form of the control-affine system. In [22], a control augmentation technique (i.e., utilizing the rate of control input as a pseudo control) was employed to create the control-affine system. However, this technique in [22] has been applied to a fixed-final-time entry guidance problem only, and an initial guess for the original control variable (i.e., the bank angle) solution was still required, which is not an easy task. Additionally, according to the discussion in [19], the control augmentation technique might be inappropriate for the entry trajectory optimization with a free-final-time problem because of the inherent nature of the problem characteristic. As another approach, a change of control variables has been utilized

to obtain the control-affine system [19]. Since the change of the control variables scheme introduces an additional nonconvex constraint on the control input variables, a relaxation technique was also suggested in this study. It has been proven that relaxed inequality guarantees the optimal solution for the original problem [19]. However, as the sub-problem infeasibility was not handled in [19], this proof was only valid for the entry trajectory optimization problem without considering the virtual control terms. Accordingly, a relatively accurate initial guess was required in this approach, and numerical integration was used to generate an initial guess of radial distance solution [19].

In this context, this paper aims to propose SCP-based entry guidance for a spaceplane, which is less sensitive to the accuracy of the initial guess and free of high-frequency jittering issues simultaneously. To this end, the characteristics of the inequality constraints, which are mainly associated with the radial distance from the center of Earth and the reentry vehicle, are investigated in the entry guidance problem. The investigation results uncover that a poor initial guess of the radial distance would be the primary source for the sub-problem infeasibility in the entry trajectory optimization problem. A single slack variable intended to relax a lower bound of the inequality conditions and a linear penalty term are used to relieve this issue while preserving the standardized convex forms. A varying bound for the trust-region constraint is also adopted further to improve the convergence performance of the successive solution procedure. Additionally, a change of control variables and a corresponding relaxation technique are utilized to form the control-affine system with the purpose of avoiding the high-frequency jittering issue in the control profile. The key property of the proposed methods lies in the fact that it is less sensitive to the accuracy of the initial guess of the radial distance solution while mitigating the high-frequency jittering issue. Therefore, the proposed methods can allow a rough initial guess. Numerical simulations are performed to verify this fact and the feasibility of the proposed methods.

The contributions of this study are threefold compared to existing results. First, the primary source for the sub-problem infeasibility in the entry trajectory optimization problem is investigated in this study, allowing us to use minimal relaxation terms to mitigate the sub-problem infeasibility. Second, more general proof of relaxation technique is provided than the previous result [19]. To be more specific, it is proven that the relaxation technique can guarantee the optimal solution for the original entry trajectory optimization problem even in the presence of the virtual control terms in this study. Last but not least, in this study, a simple linear interpolation (two straight lines connecting the boundary conditions) is proposed to generate an initial guess of radial distance solution without a computationally expensive process (i.e., numerical integration of dynamic equations), unlike the previous works [19,24].

The remainder of this paper is organized as follows: In Section 2, the entry guidance problem is formulated in the trajectory optimization framework. In Section 3, the convexification process and the modifications are discussed. In Section 4, simulation results are offered to show the performance of the proposed methods. Finally, the concluding remarks are provided in Section 5.

2. PROBLEM FORMULATION

In this study, the entry guidance problem is formulated based on the trajectory optimization framework by leveraging the concept of the computational guidance and control (CG&C) approach [13,14]. This section provides the details of the problem formulation: the equations of motion, the boundary conditions, the practical constraints, and the performance index, which is based on [19].

2.1. Equations of motion

Under the assumption of a spherical rotating Earth, the three-degree-freedom (3DOF) equations of motion for a reentry vehicle with respect to the non-dimensional time can be written as follows [34]:

$$\frac{dr}{d\tau} = V \sin \gamma, \quad (1)$$

$$\frac{d\lambda}{d\tau} = \frac{V \cos \gamma \cos \psi}{r}, \quad (2)$$

$$\frac{dl}{d\tau} = \frac{V \cos \gamma \sin \psi}{r \cos \lambda}, \quad (3)$$

$$\begin{aligned} \frac{dV}{d\tau} = & -D - \frac{\sin \gamma}{r^2} \\ & + \Omega^2 r \cos \lambda (\sin \gamma \cos \lambda - \cos \gamma \sin \lambda \cos \psi), \end{aligned} \quad (4)$$

$$\begin{aligned} \frac{d\gamma}{d\tau} = & \frac{L \cos \sigma}{V} - \left(\frac{1}{V r^2} - \frac{V}{r} \right) \cos \gamma + 2\Omega \cos \lambda \sin \psi \\ & + \frac{\Omega^2 r \cos \lambda}{V} (\cos \gamma \cos \lambda + \sin \gamma \sin \lambda \cos \psi), \end{aligned} \quad (5)$$

$$\begin{aligned} \frac{d\psi}{d\tau} = & \frac{L \sin \sigma}{V \cos \gamma} + \frac{V}{r} \cos \gamma \sin \psi \tan \lambda \\ & - 2\Omega (\tan \gamma \cos \lambda \cos \psi - \sin \lambda) \\ & + \frac{\Omega^2 r}{V \cos \gamma} \sin \lambda \cos \lambda \sin \psi, \end{aligned} \quad (6)$$

where the variable r denotes the non-dimensional radial distance between the center of Earth and the reentry vehicle. This variable representing the length quantity is scaled by the radius of Earth R_0 . The variables λ and l represent the latitude and longitude, respectively. The variable V represents the non-dimensional vehicle speed relative to Earth, which is scaled by $\sqrt{R_0 g_0}$, where g_0 is the gravitational acceleration at sea level. The variables γ and ψ represent the flight path angle and the heading angle

of the vehicle, respectively. The parameter Ω is the non-dimensional Earth rotation rate, scaled by $\sqrt{g_0/R_0}$. The variable τ is the non-dimensional time, which is defined as follows:

$$\tau \triangleq \frac{t}{\sqrt{R_0/g_0}}. \quad (7)$$

In the above equations, the terms L and D represent the aerodynamic lift and aerodynamic drag in g_0 . These are given by

$$L = \frac{1}{2m} R_0 \rho V^2 S_{\text{ref}} C_L, \quad (8)$$

$$D = \frac{1}{2m} R_0 \rho V^2 S_{\text{ref}} C_D, \quad (9)$$

where the parameters m and S_{ref} represent the dimensional vehicle mass and the dimensional reference area, which are assumed to be constant values. The parameters C_L and C_D denote the lift and drag coefficients, which are the non-dimensional values and given by the functions of the angle-of-attack α and Mach number M . In the above equations, the variable ρ denotes the dimensional air density, and it is given by

$$\rho = \rho_0 e^{-h/h_s}, \quad (10)$$

where $h \triangleq rR_0 - R_0$ is the altitude relative to Earth. The parameter ρ_0 is the air density at sea level, and the parameter h_s denotes the reference altitude for the exponential air density model. The definition of the state variables is shown in Fig. 1. In orbital mechanics, the negative of the specific mechanical energy [12] can be written as

$$e \triangleq \frac{1}{r} - \frac{V^2}{2}. \quad (11)$$

By differentiating e with respect to the non-dimensional time τ , we have

$$\frac{de}{d\tau} = -\frac{1}{r^2} \frac{dr}{d\tau} - V \frac{dV}{d\tau}. \quad (12)$$

Under the small value assumption of Ω in (4) (i.e., $\Omega \approx 0$), the above equation can be approximated as

$$\frac{de}{d\tau} \approx DV > 0. \quad (13)$$

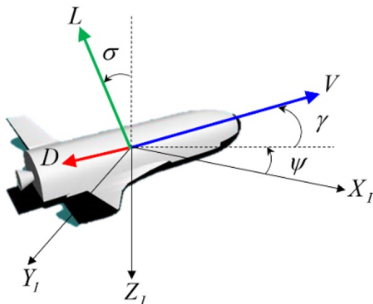


Fig. 1. The definition of the state variables.

From (13), it is worth noting that e is monotonically increasing with respect to τ . This fact implies that e can be used as the independent variable instead of τ . Additionally, as the definition of e is given by the function of r and V , the equation of motion for the vehicle speed can be dropped if e is used as the independent variable. It could be an advantage in terms of relieving the complexity of the state equations in a way to reduce the size of the state vectors. By applying (13) to the original equations of motion, the non-dimensional 3DOF (degree-of-freedom) equations of motion with respect to the specific energy can be written as

$$\frac{dr}{de} = \frac{\sin \gamma}{D}, \quad (14)$$

$$\frac{d\lambda}{de} = \frac{\cos \gamma \cos \psi}{rD}, \quad (15)$$

$$\frac{dl}{de} = \frac{\cos \gamma \sin \psi}{rD \cos \lambda}, \quad (16)$$

$$\begin{aligned} \frac{d\gamma}{de} = & \frac{L \cos \sigma}{V^2 D} + \left(V^2 - \frac{1}{r} \right) \frac{\cos \gamma}{r V^2 D} + \frac{2\Omega \cos \lambda \sin \psi}{VD} \\ & + \frac{\Omega^2 r \cos \lambda}{V^2 D} (\cos \gamma \cos \lambda + \sin \gamma \sin \lambda \cos \psi), \end{aligned} \quad (17)$$

$$\begin{aligned} \frac{d\psi}{de} = & \frac{L \sin \sigma}{V^2 D \cos \gamma} + \frac{1}{Dr} \cos \gamma \sin \psi \tan \lambda \\ & - 2\Omega (\tan \gamma \cos \lambda \cos \psi - \sin \lambda) \frac{1}{VD} \\ & + \frac{\Omega^2 r}{V^2 D \cos \gamma} \sin \lambda \cos \lambda \sin \psi. \end{aligned} \quad (18)$$

From (11), as the definition of e is given by the function of r and V , and the non-dimensional vehicle speed can be directly determined from the given independent variables e and r as

$$V = \sqrt{2 \left(\frac{1}{r} - e \right)}. \quad (19)$$

2.2. Control inputs

Most reentry vehicles have adopted the bank-to-turn (BTT) control system, as shown in Fig. 2. The magnitude of lift L and lift direction can be considered the control inputs in BTT control. In most reentry vehicles, the angle-of-attack is controlled to follow the predetermined angle-of-attack profile for ensuring thermal protection and trimmed flight. Therefore, only the bank angle σ becomes the control input for a reentry vehicle. As shown in Fig. 2, the lift L with the bank angle σ can be decomposed into the vertical $L \cos \sigma$ and horizontal forces $L \sin \sigma$, respectively. These two forces can introduce the changes in the flight path angle and the heading angle, as shown in (17) and (18). The system equation can then be regarded as a control-affine system with respect to these control forces.

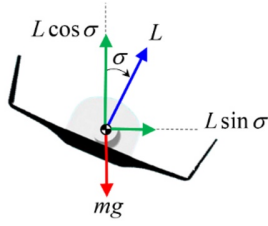


Fig. 2. The bank-to-turn control mechanism.

It is well-known that the control-affine system is more desirable for avoiding unwanted high-frequency jittering issues in the successive linearization procedure [19,35]. Accordingly, new control variables to exploit the benefit of the control-affine system [20,35] are defined as follows:

$$a_h \triangleq L \sin \sigma, \quad a_v \triangleq L \cos \sigma. \quad (20)$$

Since the new control variables a_h and a_v are not independent, the following kinematics rule should be met.

$$a_h^2 + a_v^2 = L^2. \quad (21)$$

For given a_h and a_v , the original bank angle can be reconstructed as

$$\sigma = \tan^{-1} \frac{a_h}{a_v}. \quad (22)$$

Note that the lift term L in (20) and (21) can be regarded as a function of the vehicle speed as the predetermined angle-of-attack profile depends on the vehicle speed.

2.3. Boundary conditions

Generally, the entry guidance phase starts at the entry interface point (EIP), and it proceeds until the terminal energy management phase (TAEM) begins. Therefore, the entry trajectory should satisfy these boundary conditions. In this study, it is assumed that the initial conditions at EIP are given as

$$\begin{aligned} r(e_0) &= r_0, \quad \lambda(e_0) = \lambda_0, \quad l(e_0) = l_0, \\ \gamma(e_0) &= \gamma_0, \quad \psi(e_0) = \psi_0, \end{aligned} \quad (23)$$

where the parameter e_0 represents the specific mechanical energy at EIP, and this value can be determined using (11) with the EIP conditions r_0 and V_0 . Additionally, the final conditions at the beginning of the TAEM phase are typically given by

$$\begin{aligned} r(e_f) &= r_f, \quad \lambda(e_f) = \lambda_f, \quad l(e_f) = l_f, \\ \gamma(e_f) &= \gamma_f, \quad \psi(e_f) = \psi_f. \end{aligned} \quad (24)$$

Likewise, the parameter e_f represents the specific mechanical energy at the beginning of the TAEM phase. It can be calculated by utilizing (11) with r_f and V_f . In this study, the final boundary conditions for the latitude and

longitude are handled as the soft constraints for improving the convergence of the successive linearization procedure as

$$|\lambda(e_f) - \lambda_f| \leq \varepsilon_\lambda, \quad |l(e_f) - l_f| \leq \varepsilon_l. \quad (25)$$

Note that if the upper bounds ε_λ and ε_l approach zero, the soft constraints in (25) gradually become the hard constraints in (24).

2.4. Flight constraints

The key benefit of the trajectory optimization-based guidance is that it allows imposing several practical flight constraints to the problem formulation. In this study, we consider commonly used constraints in the entry guidance problem. The first constraint to be considered is the maximum heat flux limit, which is essential to protect the vehicle material from aerodynamic heating [36]. This constraint is typically modeled as

$$\dot{Q}_{\max} \geq C_q \sqrt{g_0 R_0^{3.15}} \sqrt{\rho} V^{3.15}. \quad (26)$$

The following constraint is the maximum dynamic pressure limit. This constraint is required to relieve the hinge moment acting on the aerodynamic control fins and prevent structural damage to the vehicle body. This constraint is given by

$$q_{\max} \geq \frac{1}{2} g_0 R_0 \rho V^2. \quad (27)$$

Another constraint is related to the maximum aerodynamic load on the vehicle body, which is given by

$$n_{\max} \geq \frac{1}{2m} R_0 \rho V^2 S_{\text{ref}} |C_Z|, \quad (28)$$

where the parameter $C_Z \triangleq C_L \cos \alpha + C_D \sin \alpha$ is the aerodynamic coefficient for the normal force. The above constraint is introduced to prevent the structural damage caused by excessive aerodynamic forces acting on the vehicle body. Note that the above constraints, as given in (26), (27), and (28), are given by the function of the air density ρ , and the air density, as given in (10), is given by the function of the radial distance r . Therefore, by substituting (10) into (26), (27), and (28) and rearranging the results with respect to the radial distance, the above constraints can be rewritten as

$$r \geq 1 - \frac{h_s}{R_0} \ln \left(\frac{\dot{Q}_{\max}^2}{\rho_0 C_q^2 (g_0 R_0)^{3.15} V^{6.3}} \right), \quad (29)$$

$$r \geq 1 - \frac{h_s}{R_0} \ln \left(\frac{2q_{\max}}{\rho_0 g_0 R_0 V^2} \right), \quad (30)$$

$$r \geq 1 - \frac{h_s}{R_0} \ln \left(\frac{2mn_{\max}}{\rho_0 R_0 V^2 S_{\text{ref}} |C_Z|} \right). \quad (31)$$

Note that the right-hand side terms of (29), (30), and (31) are given by the function of the vehicle speed V and the parameters \dot{Q}_{\max} , C_q , q_{\max} , and n_{\max} . These parameters are depending on the reentry vehicle designs. In this study, we assume that these parameters are given.

Additionally, the allowable bank angle is typically bounded because of the maneuverability characteristics of the reentry vehicle as

$$\sigma_{\min} \leq |\sigma| \leq \sigma_{\max}. \quad (32)$$

Accordingly, the control input is constrained as

$$L \cos \sigma_{\max} \leq a_v \leq L \cos \sigma_{\min}. \quad (33)$$

2.5. Minimum-time guidance problem

In this study, the minimum-time entry guidance problem is mainly considered with the purpose of minimizing the heat accumulation during a reentry flight. The performance index for the flight time with respect to the specific mechanical energy can be written as

$$J = \int_{\tau_0}^{\tau_f} 1 d\tau = \int_{e_0}^{e_f} \frac{1}{DV} de. \quad (34)$$

To enforce the soft constraints in (25) to become the hard constraints (24), the parameters ε_λ and ε_l should be minimized. In this context, the optimal guidance problem can be formulated as follows:

$$\begin{aligned} P_1 : \min J &= c_\lambda \varepsilon_\lambda + c_l \varepsilon_l + \int_{e_0}^{e_f} \frac{1}{DV} de \\ &\text{subject to (14)-(19), (21), (23)-(25),} \\ &\quad \text{(29)-(31), (33).} \end{aligned} \quad (35)$$

For convenience, the above problem is called P_1 in this study. In the problem P_1 , the vertical force a_v and horizontal force a_h can be considered as the free variables to be optimized. Furthermore, the equations of motion and the performance index are nonlinear, and there are nonconvex constraints. Accordingly, this problem can be characterized as a nonconvex problem.

3. SECOND-ORDER CONE PROGRAMMING WITH LINEAR PENALIZATION

This section elaborates on the convexification process for the original problem P_1 based on the successive linearization [20] and other convexification techniques. After performing convexification, the problem P_1 is converted into the SOCP sub-problems. The sub-problem infeasibility issue with a poor initial guess is investigated. To resolve this issue, a relaxation technique is also applied to the SOCP sub-problems.

3.1. System equation

For notational convenience, let the state vector and the input vector be defined as follows:

$$x \triangleq [r, \lambda, l, \gamma, \psi]^T, \quad u \triangleq [a_v, a_h]^T. \quad (36)$$

Based on the definitions of the state vector and the input vector, the system equation can be expressed as

$$x' = f_1(x) + h(x)u + f_2(x), \quad (37)$$

where

$$f_1(x) \triangleq \begin{bmatrix} \frac{\sin \gamma}{D} \\ \frac{\cos \gamma \cos \psi}{rD} \\ \frac{\cos \gamma \sin \psi}{rD \cos \lambda} \\ \left(V^2 - \frac{1}{r}\right) \frac{\cos \gamma}{rV^2 D} \\ \frac{\cos \gamma \sin \psi \tan \lambda}{rD} \end{bmatrix}, \quad h(x) \triangleq \begin{bmatrix} 0 & 0 \\ 0 & 0 \\ 0 & 0 \\ \frac{1}{V^2 D} & 0 \\ 0 & \frac{1}{V^2 D \cos \gamma} \end{bmatrix}, \quad (38)$$

where x' represents the differentiation of the state vector with respect to e . The remaining terms with Ω in (14) to (18) are defined as the function $f_2(x)$. It is worth pointing out that the system equation is given in the form of the control-affine system.

3.2. Convexification process

In the optimal control problem, the system equation can be considered as a set of equality constraints. Since the system equation is highly nonlinear, as shown in (37) and (38), these constraints are nonconvex. Accordingly, the successive linearization technique is first applied to the nonlinear system equation. The basic idea of the successive linearization is to sequentially linearize nonlinear terms at a previous iteration solution by leveraging a first-order Taylor series approximation. Assuming that the i -th iteration solutions are given as $x^{(i)} = [r^{(i)}, \lambda^{(i)}, l^{(i)}, \gamma^{(i)}, \psi^{(i)}]^T$ and $u^{(i)} = [a_v^{(i)}, a_h^{(i)}]^T$. According to the Taylor theorem, the linear approximation of the nonlinear term $f_1(x)$ near the i -th iteration solutions is written as

$$f_1(x) \approx f_1(x^{(i)}) + \frac{\partial f_1(x^{(i)})}{\partial x} (x - x^{(i)}). \quad (39)$$

Note that the above approximation is valid only in a sufficiently small neighborhood of $x = x^{(i)}$ as

$$\|x - x^{(i)}\| \leq \delta. \quad (40)$$

It is called the trust-region constraint, where δ is the upper bound. Furthermore, as the variations of $h(x)$ and $f_2(x)$ according to changes in the state vector x are insignificant, these terms can also be approximated by the lagging technique (i.e., the function values are determined by directly assigning the previous iteration solutions) [37].

$$h(x) \approx h(x^{(i)}), \quad f_2(x) \approx f_2(x^{(i)}). \quad (41)$$

By utilizing these approximations, the nonlinear system equation can be written in a linear form as

$$x' \approx F_x(x^{(i)})x + h(x^{(i)})u + R(x^{(i)}), \quad (42)$$

where

$$F_x(x^{(i)}) \triangleq \frac{\partial f_1(x^{(i)})}{\partial x}, \quad (43)$$

$$R(x^{(i)}) \triangleq f_1(x^{(i)}) - \frac{\partial f_1(x^{(i)})}{\partial x}x^{(i)} + f_2(x^{(i)}). \quad (44)$$

Note that the terms $F_x(x^{(i)})$, $h(x^{(i)})$ and $R(x^{(i)})$ are constant matrices because these are given by the function of the previous iteration solutions. Thus, the system equation in (42) becomes a linear function, and it will be converted into a set of convex equality constraints after performing discretization.

Hereafter, let us discuss the convexification process for nonconvex constraints. As the flight constraints, as shown in (29), (30), and (31) are given by the function of the vehicle speed (which is further given by the function of the non-dimensional radial distance r and the specific mechanical energy e), these are implicitly nonconvex constraints. Therefore, by applying the lagging technique, these inequality constraints can be approximated as

$$r \geq 1 - \frac{h_s}{R_0} \ln \left(\frac{Q_{\max}^2}{\rho_0 C_q^2 (g_0 R_0)^{3.15} (V^{(i)})^{6.3}} \right), \quad (45)$$

$$r \geq 1 - \frac{h_s}{R_0} \ln \left(\frac{2q_{\max}}{\rho_0 g_0 R_0 (V^{(i)})^2} \right), \quad (46)$$

$$r \geq 1 - \frac{h_s}{R_0} \ln \left(\frac{2mn_{\max}}{\rho_0 R_0 (V^{(i)})^2 S_{\text{ref}} |C_Z(V^{(i)})|} \right), \quad (47)$$

where the parameter $V^{(i)}$ is given by

$$V^{(i)} = \sqrt{2 \left(\frac{1}{r^{(i)}} - e \right)}. \quad (48)$$

Next, the kinematics constraints for the control inputs can be convexified by the relaxation [20] and the lagging techniques as follows:

$$a_h^2 + a_v^2 \leq L(V^{(i)})^2. \quad (49)$$

Furthermore, the control input constraints, as shown in (33), can be approximated by the lagging technique as

$$L(V^{(i)}) \cos \sigma_{\max} \leq a_v \leq L(V^{(i)}) \cos \sigma_{\min}. \quad (50)$$

Note that the upper or lower bounds in (45), (46), (47), (49), and (50) are constant values as these are given by the function of the previous iteration solutions $x^{(i)}$.

Lastly, as the integrand of the performance index, as given in (35), is nonlinear, it should be convexified. Based on the successive linearization, the nonlinear integrand can be approximated from (9), (10), and (35), as follows:

$$\frac{1}{DV} \approx \eta_1(x^{(i)})r + \eta_0(x^{(i)}), \quad (51)$$

where

$$\eta_1(x^{(i)}) \triangleq \frac{2m}{\rho^{(i)} h_s S_{\text{ref}} (V^{(i)})^3 C_D(V^{(i)})}, \quad (52)$$

$$\eta_0(x^{(i)}) \triangleq -\frac{2mr^{(i)}}{\rho^{(i)} h_s S_{\text{ref}} (V^{(i)})^3 C_D(V^{(i)})} + \frac{2m}{\rho^{(i)} R_0 S_{\text{ref}} (V^{(i)})^3 C_D(V^{(i)})}, \quad (53)$$

$$\rho^{(i)} \triangleq \rho_0 e^{-\frac{(r^{(i)} R_0 - R_0)}{h_s}}. \quad (54)$$

Note that the terms $\eta_0(x^{(i)})$ and $\eta_1(x^{(i)})$ are assumed to be constant values given by the function of the i -th previous iteration solutions $x^{(i)}$.

3.3. Discretization

This section explains the discretization procedure for the linearized system equation. It is the process of transforming the linearized system equation, as given in (42), into a set of equality constraints. The independent variable e is discretized into $N_k + 1$ uniformly distributed points as

$$e_k = e_0 + k\Delta e, \quad \forall k \in [0, N_k], \quad (55)$$

where $\Delta e \triangleq (e_f - e_0) / N_k$. Then, the state and the control input vector at the k -th step can be defined as

$$x_k \triangleq x(e_k) = [r_k, \lambda_k, l_k, \gamma_k, \psi_k]^T, \\ u_k \triangleq u(e_k) = [a_{v,k}, a_{h,k}]^T. \quad (56)$$

Likewise, for notational convenience, the terms $F_x(x^{(i)})$, $h(x^{(i)})$, and $R(x^{(i)})$ at the k -th step are defined as

$$F_{x,k}^{(i)} = F_x(x^{(i)}(e_k)), \quad h_k^{(i)} = h(x^{(i)}(e_k)), \\ R_k^{(i)} = R(x^{(i)}(e_k)). \quad (57)$$

Based on the trapezoidal numerical method, the linearized system equation can be numerically integrated as follows:

$$x_{k+1} = x_k + \frac{(x'_{k+1} + x'_k)}{2} \Delta e, \quad \forall k \in [0, N_k - 1]. \quad (58)$$

By substituting (42) into (58) and rearranging the result, we have

$$A_{k+1}x_{k+1} + B_{k+1}u_{k+1} + C_{k+1} \\ = A_k x_k + B_k u_k + C_k, \quad \forall k \in [0, N_k - 1], \quad (59)$$

where

$$\begin{aligned} A_{k+1} &\triangleq I - \frac{\Delta e}{2} F_{x,k+1}^{(i)}, B_{k+1} \triangleq -\frac{\Delta e}{2} h_{k+1}^{(i)}, \\ C_{k+1} &\triangleq -\frac{\Delta e}{2} R_{k+1}^{(i)}, \end{aligned} \quad (60)$$

$$A_k \triangleq I + \frac{\Delta e}{2} F_{x,k}^{(i)}, B_k \triangleq \frac{\Delta e}{2} h_k^{(i)}, C_k \triangleq \frac{\Delta e}{2} R_k^{(i)}, \quad (61)$$

where the parameter I represents an identity matrix with the same dimension as N_s . Additionally, the linearized integrand of the performance index, as shown in (51), can be discretized as follows:

$$\begin{aligned} &\int_{e_0}^{e_f} \left[\eta_1 \left(x^{(i)} \right) r + \eta_0 \left(x^{(i)} \right) \right] de \\ &\approx \sum_{k=0}^{N_k} (\Gamma_{1,k} r_k + \Gamma_{0,k}) \Delta e, \end{aligned} \quad (62)$$

where

$$\Gamma_{1,k} \triangleq \eta_1 \left(x^{(i)}(e_k) \right), \quad \Gamma_{2,k} \triangleq \eta_0 \left(x^{(i)}(e_k) \right). \quad (63)$$

Lastly, in the discrete-energy domain $\forall k \in [0, N_k]$, the above constraints can also be written as

$$r_k \geq 1 - \frac{h_s}{R_0} \ln \left(\frac{\dot{Q}_{\max}^2}{\rho_0 C_q^2 (g_0 R_0)^{3.15} \left(V_k^{(i)} \right)^{6.3}} \right), \quad (64)$$

$$r_k \geq 1 - \frac{h_s}{R_0} \ln \left(\frac{2q_{\max}}{\rho_0 g_0 R_0 \left(V_k^{(i)} \right)^2} \right), \quad (65)$$

$$r_k \geq 1 - \frac{h_s}{R_0} \ln \left(\frac{2mn_{\max}}{\rho_0 R_0 \left(V_k^{(i)} \right)^2 S_{\text{ref}} |C_Z \left(V_k^{(i)} \right)|} \right), \quad (66)$$

$$\left| x_k - x_k^{(i)} \right| \leq \delta, \quad (67)$$

$$a_{v,k}^2 + a_{h,k}^2 \leq L_k^2, \quad (68)$$

$$L_k \cos \sigma_{\max} \leq a_{v,k} \leq L_k \cos \sigma_{\min}, \quad (69)$$

$$r_0^{(i)} = r_0, \lambda_0^{(i)} = \lambda_0, l_0^{(i)} = l_0, \gamma_0^{(i)} = \gamma_0, \psi_0^{(i)} = \psi_0, \quad (70)$$

$$\begin{aligned} r_{N_k}^{(i)} &= r_f, \gamma_{N_k}^{(i)} = \gamma_f, \psi_{N_k}^{(i)} = \psi_f, \\ \left| \lambda_{N_k}^{(i)} - \lambda_f \right| &\leq \varepsilon_\lambda, \left| l_{N_k}^{(i)} - l_f \right| \leq \varepsilon_l, \end{aligned} \quad (71)$$

where $L_k \triangleq L \left(V_k^{(i)} \right)$.

3.4. Convex sub-problems

In this subsection, the convex sub-problem is formulated in the form of SOCP. Based on the successive convexification process, the convex sub-problem can be constructed as follows:

$$P_2: \min J = c_\lambda \varepsilon_\lambda + c_l \varepsilon_l + \sum_{k=0}^{N_k} (\Gamma_{1,k} r_k + \Gamma_{0,k}) \Delta e$$

subject to (64)-(71). (72)

From (72), it can be readily observed that the above problem belongs to the SOCP problem, and it can be solved by the generic sequential convex programming (SCP) method. For convenience, the above problem is called the problem P_2 in this study.

3.5. Modified convex sub-problems

In this subsection, the modified convex sub-problem is constructed to enhance the convergence characteristics of the generic SCP approach. As discussed in the Introduction, the sub-problem infeasibility occurs when an initial guess is inaccurate in the generic SCP method. This issue becomes more severe in most entry guidance problems. As the system equation is given in the form of the control-affine system, as shown in (37), an initial guess for the control inputs is not required. Besides, it is worth noting that among the inequality constraints in the entry guidance problem, the inequality constraints associated with the maximum heat flux limit, the maximum dynamic pressure limit, and the maximum load factor limit, as shown in (64), (65), and (66), are highly related to an initial guess for the state variable r . Hence, if an initial guess for r is poor, the early iteration solutions often lie outside of these inequality constraints during the successive linearization process. Accordingly, the sub-problem infeasibility arises. To be more specific, one of rough initial guess options for the radial distance r would be a straight line connecting its initial boundary condition and final boundary condition (or a combination of straight lines connecting intermediate points). Without loss of generality, it can be expressed in a linear function (or a set of linear functions) as follows:

$$r_k^{(0)} = ae_k + b, \quad \forall k \in [0, N_k], \quad (73)$$

where a and b are constant values, and these are given by

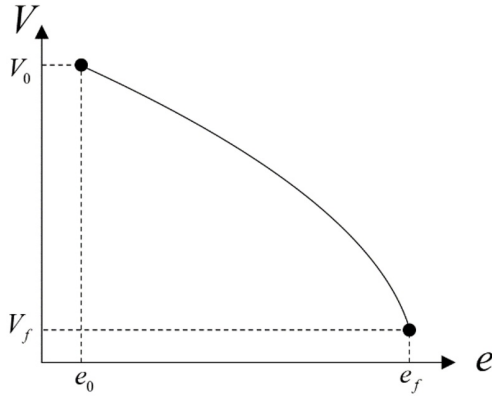
$$a \triangleq \frac{r_f - r_0}{e_f - e_0}, \quad b \triangleq r_0 - ae_0. \quad (74)$$

Note that the parameter a can be considered as the slope of this linear function, and it has a negative value $a < 0$. From (19) and (74), the vehicle speed at the k -th step can be determined as

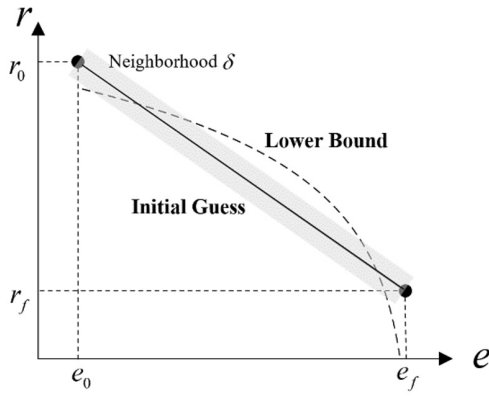
$$\begin{aligned} V_k^{(0)} &= \sqrt{2 \left(\frac{1}{r_k^{(0)}} - e_k \right)} \\ &= \sqrt{2 \left(\frac{1}{ae_k + b} - e_k \right)}, \quad \forall k \in [0, N_k]. \end{aligned} \quad (75)$$

The lower bounds of the inequality constraints associated with r at the k -th step can be expressed in the generic forms as

$$r_{LB,k}^{(0)} = 1 - p_1 \ln \left(p_2 \frac{1}{\left(V_k^{(0)} \right)^2} \right) \text{ or}$$



(a) Vehicle speed.



(b) Radial distance and its bounds.

Fig. 3. The general patterns of vehicle speed, radial distance, and its bounds.

$$r_{LB,k}^{(0)} = 1 - p_1 \ln \left(p_2 \frac{1}{\left(V_k^{(0)}\right)^{6.3}} \right), \quad (76)$$

where the parameters p_1 and p_2 are given by the function of the parameters \dot{Q}_{\max} , C_q , q_{\max} , and n_{\max} . The general pattern of the vehicle speed can be depicted as shown in Fig. 3(a), and the general pattern of the lower bounds and the initial guess for the radial distance can be visualized as depicted in Fig. 3(b). The general pattern of the lower bound for the inequality constraints regarding r is curved towards the upper right corner, as shown in Fig. 3(b). Thus, in the next iteration, the possible solution within the trust-region bound δ might lie in infeasible solution space if the rough initial guess for r (i.e., a straight line connecting the two boundary conditions) is used, and the sub-problems infeasibility occurs.

To relax the above issue, the slack variable is augmented to the inequality constraints as shown in (64), (65), and (66) as

$$r_k \geq 1 - \frac{h_s}{R_0} \ln \omega_k - v_k \quad \forall k \in [0, N_k], \quad (77)$$

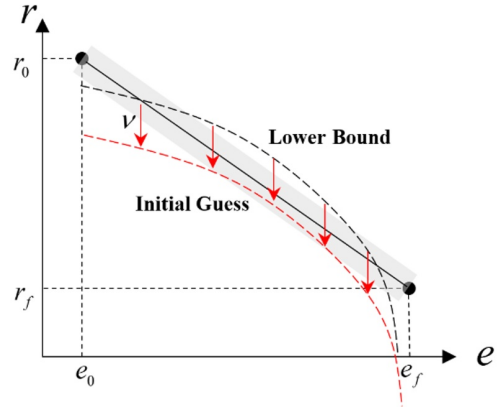


Fig. 4. The visualization for the effect of lower bound relaxation.

$$v_k \geq 0, \quad \forall k \in [0, N_k], \quad (78)$$

where

$$\begin{aligned} \omega_k &= \min(\omega_{k,1}, \omega_{k,2}, \omega_{k,3}), \\ \omega_{k,1} &\triangleq \frac{\dot{Q}_{\max}^2}{\rho_0 C_q^2 (g_0 R_0)^{3.15} \left(V_k^{(i)}\right)^{6.3}}, \\ \omega_{k,2} &\triangleq \frac{2q_{\max}}{\rho_0 g_0 R_0 \left(V_k^{(i)}\right)^2}, \\ \omega_{k,3} &\triangleq \frac{2mn_{\max}}{\rho_0 R_0 \left(V_k^{(i)}\right)^2 S_{\text{ref}} \left|C_Z \left(V_k^{(i)}\right)\right|}. \end{aligned} \quad (79)$$

The role of this slack variable is to bring the effect of making the lower bound move downward direction, as shown in Fig. 4. In this way, the possible solution within the trust-region bound can be in a feasible solution space in the next iteration. To enforce the relaxed constraint to become the original constraint, the magnitudes of the slack variable should be zero as the iteration proceeds. In this context, the slack variable is included in the performance index as a linear penalty term.

$$v \triangleq \sum_{k=0}^{N_k} v_k. \quad (80)$$

Furthermore, the trust-region bound is essential for the convergence and feasibility characteristics of the SCP method. Although a hard trust-region constraint with a fixed bound in (67) would be suitable for retaining a sufficient step size at every iteration, it might be more vulnerable for a poor initial guess. On the other hand, a soft trust-region constraint with a varying bound [29] is beneficial to ensure the bounded and feasible solutions for a poor initial guess. Thus, a trust-region constraint with a varying term is adopted in this study further to improve

the convergence performance of the successive convexification procedure.

$$\begin{aligned} |x_k - x_k^{(i)}| &\leq \delta_1^{(i)}, \forall k \in [0, N_k], \\ \delta_1^{(i)} &\geq 0, \end{aligned} \quad (81)$$

where $\delta_1^{(i)}$ represents a varying bound at the i -th iteration. To mitigate the effect of the varying bound in (81), the term $\delta_1^{(i)}$ needs to be zero as the iteration proceeds. Thus, this term is augmented into the performance index. Finally, the modified convex sub-problem can be formulated as follows:

$$\begin{aligned} P_3 : \min J &= c_\lambda \varepsilon_\lambda + c_l \varepsilon_l + \sum_{k=0}^{N_k} (\Gamma_{1,k} r_k + \Gamma_{0,k}) \Delta e \\ &+ w_v \sum_{k=0}^{N_k} v_k + w_\delta \delta_1 \\ \text{subject to} & \text{ (68)-(71), (77)-(81),} \end{aligned} \quad (82)$$

where w_v and w_δ are weight values for the penalty term. For convenience, the above problem is called the problem P_3 in this study. It can be effectively solved by the successive convexification algorithm, which will be explained in the following subsection. Additionally, as proven in Proposition 1, the optimal solution with the relaxation technique used in (49) will be the same as the optimal solution for the original problem.

Proposition 1: Whenever the sub-problem P_3 is solved, the convex relaxation holds. i.e., $a_v^2(e) + a_h^2(e) = L(V^{(i)})^2$ almost everywhere on $[e_0, e_f]$.

Proof: See Appendices A and B. \square

Remark 1: Proposition 1 is a more general statement of a relaxation technique than the previous study [19] because it is proven that the relaxation technique can guarantee the optimal solution for the original entry trajectory optimization problem even in the presence of the slack variables (virtual control terms). Besides, a regularization term in the performance index is not required in the proof procedure, unlike the previous study [19].

3.6. Successive convexification algorithm

This subsection describes the successive convexification procedure used in this study. The successive convexification algorithm solves the convex sub-problem formulated in (82) iteratively until the predetermined convergence criterion is met. The details of the successive convexification procedure are summarized in Algorithm 1.

As shown in Algorithm 1, the initial guess for the first iteration solutions $x^{(0)}$ is required in this approach. In this study, a rough initial guess, which are straight lines connecting the initial boundary conditions and the final boundary conditions, is used as follows:

$$\lambda_k^{(0)} = \mu_{1,k} \lambda_0 + \mu_{2,k} \lambda_f, \forall k \in [0, N_k],$$

Algorithm 1: Successive convexification.

Input: An initial guess of solution $x^{(0)}$ and initial weight values w_v and w_δ

for all $i = 0 : N_{\max}$ **do**

solve a convex sub-problem (82) with $x^{(i)}$

if $\max |x^{(i+1)} - x^{(i)}| \leq \varepsilon_{tol}$ **then**

Return $x^{(i+1)}$ and $u^{(i+1)}$

end if

end for

$$\begin{aligned} l_k^{(0)} &= \mu_{1,k} l_0 + \mu_{2,k} l_f, \forall k \in [0, N_k], \\ \gamma_k^{(0)} &= \mu_{1,k} \gamma_0 + \mu_{2,k} \gamma_f, \forall k \in [0, N_k], \\ \psi_k^{(0)} &= \mu_{1,k} \psi_0 + \mu_{2,k} \psi_f, \forall k \in [0, N_k], \end{aligned} \quad (83)$$

where $\mu_{1,k}$ and $\mu_{2,k}$ are defined as

$$\mu_{1,k} \triangleq \frac{N_k - k}{N_k}, \mu_{2,k} \triangleq \frac{k}{N_k}, \forall k \in [0, N_k]. \quad (84)$$

For an initial guess of r , two straight lines connecting the initial boundary conditions, intermediate points, and the final boundary conditions, are used as follows:

$$r_k^{(0)} = \begin{cases} \mu_{11,k} r_0 + \mu_{12,k} r_{\text{ref}}, & \text{if } k \leq N_{\text{ref}}, \\ \mu_{21,k} r_{\text{ref}} + \mu_{22,k} r_f, & \text{otherwise,} \end{cases} \forall k \in [0, N_k], \quad (85)$$

with

$$\begin{aligned} \mu_{11,k} &\triangleq \frac{N_{\text{ref}} - k}{N_{\text{ref}}}, \mu_{21,k} \triangleq \frac{N_k - N_{\text{ref}} - k}{N_k - N_{\text{ref}}}, \\ \mu_{12,k} &\triangleq \frac{k}{N_{\text{ref}}}, \mu_{22,k} \triangleq \frac{k}{N_k - N_{\text{ref}}}, \forall k \in [0, N_k], \end{aligned} \quad (86)$$

where $r_{\text{ref}} \triangleq (R_0 + h_{\text{ref}})/R_0$. It will be shown in simulation results that this initial guess can ensure a good convergence characteristic because the linear penalization can help resolve the infeasibility issue at the early iteration due to a poor initial guess.

Remark 2: Although the convergence of the successive convexification procedure is not rigorously proved yet, its usefulness and efficiency have been successfully demonstrated through extensive studies on this method. It has also been successfully applied to a real application: reusable rocket landing guidance [28].

4. SIMULATION RESULTS

In this section, numerical simulations are conducted to show the performance of the proposed methods. A reentry vehicle model and an environment model used in this study are introduced. The design parameters for the proposed method are then described. Lastly, the numerical optimization results are offered.

4.1. Reentry vehicle model and environment model

A reentry vehicle model used in this study refers to [23], where the vehicle mass is 104,305 kg, and the reference area is 391.22 m². The aerodynamic coefficients for the reentry vehicle [8] are given by

$$C_L = -0.041065 + 0.016292\alpha + 0.00026024\alpha^2, \quad (87)$$

$$C_D = 0.080505 - 0.03026C_L + 0.86495C_L^2, \quad (88)$$

where α is in degrees. Here, the angle-of-attack α is controlled to track the predetermined speed-dependent profile. The reference angle-of-attack profile with respect to the vehicle speed is given by [8]

$$\alpha = \begin{cases} 40 \text{ deg}, & \text{if } v \geq 4570 \text{ m/s}, \\ -0.0073(4570 - v) + 40 \text{ deg}, & \text{if } 760 \leq v < 4570 \text{ m/s}, \\ 12 \text{ deg}, & \text{otherwise,} \end{cases} \quad (89)$$

where $v \triangleq V\sqrt{g_0 R_0}$ is the dimensional vehicle speed. From [23], the parameters for the flight path constraints in (26), (27), and (28) are chosen as follows: $\dot{Q}_{\max} = 1,500$ kW/m², $C_q = 1.65 \times 10^{-4}$ W/m², $q_{\max} = 18,000$ N/m², and $n_{\max} = 2.5$ g. Additionally, the parameters for the bank angle constraints in (32) are selected as $\sigma_{\min} = 15$ deg and $\sigma_{\max} = 165$ deg. In this study, a simple exponential atmosphere model with $\rho_0 = 1.225$ kg/m³ and $h_s = 8.42$ km is used. The values for the radius of Earth, the gravitational acceleration at sea-level, and the dimensional Earth rotation rate are selected as $R_0 = 6379.137$ km, $g_0 = 9.81$ m/s², and $\Omega = 7.292115 \times 10^{-5}$ rad/s, respectively.

4.2. Simulation conditions

For the entry mission considered in this study, the initial boundary condition at the entry interface point and the final condition are provided in Table 1. In the entry trajectory optimization, it is assumed that the trajectory is discretized into 201 evenly distributed points (i.e., $N_k = 200$). The design parameters for the proposed methods are set to $w_v = 100$, $w_\delta = 1$, $c_\lambda = 10$, and $c_l = 10$, respectively. For the initial guess, the parameters N_{ref} and h_{ref} are chosen as $N_{\text{ref}} = 5$ and $h_{\text{ref}} = 85$ km. The stopping criterion for the successive convexification procedure in Algorithm 1 is set to

$$\epsilon_{\text{tol}} = \left[\frac{200}{R_0}, \frac{0.05\pi}{180}, \frac{0.05\pi}{180}, \frac{0.05\pi}{180}, \frac{0.05\pi}{180} \right]^T. \quad (90)$$

Additionally, in the trajectory optimization, MATLAB in conjunction with MOSEK [38] (which is the most advanced SOCP solver) is utilized to solve convex sub-problems. All the results are obtained by implementing the software tools and the algorithm on a desktop with Intel (R) Core i7-8700 3.20 GHz.

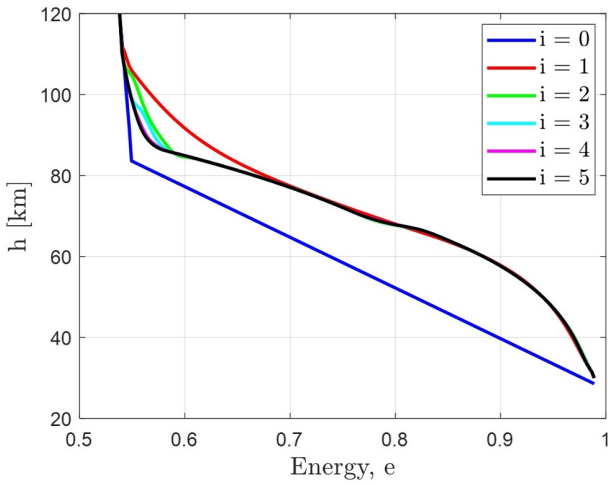
Table 1. The parameters for entry trajectory optimization.

Parameter	Value	Parameter	Value
V_0	7450 m/s	V_f	900 m/s
h_0	120 km	h_f	30 km
λ_0	29.4692 deg	λ_f	37.4692 deg
l_0	79.4510 deg	l_f	126.4510 deg
γ_0	-0.5 deg	γ_f	-5.0 deg
ψ_0	90 deg	ψ_f	-90 deg

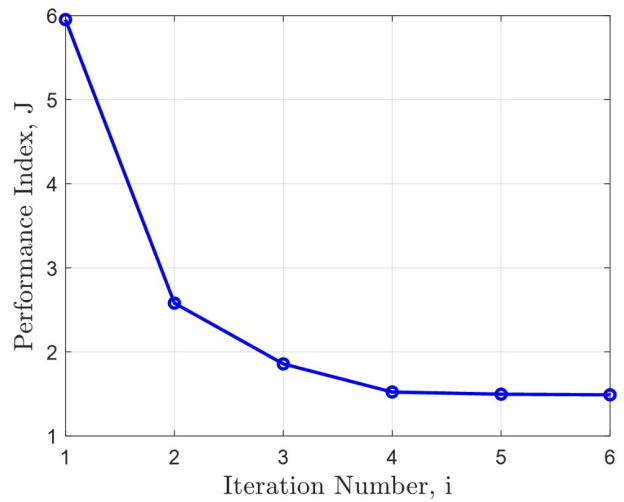
4.3. Simulation results

In the entry trajectory optimization, six successive iterations are conducted to obtain the converged complete solution. By utilizing MOSEK, it takes about 0.2 seconds to solve the problem P_3 , as formulated in Subsection 3.5. Note that it is a promising result for online implementation potential: if a customized SOCP solver written in C language is utilized, the computation time could be further reduced. To examine the convergence characteristics of the successive convexification process with the proposed relaxations, altitude and bank angle profiles in successive iterations are plotted as shown in Fig. 5. The results obtained readily show that the altitude and bank angle profiles are almost converged within three or four successive iterations despite the fact that a rough initial guess (i.e., straight lines connecting initial and final conditions) is used. These results confirm a rapid convergence feature of the proposed methods. Additionally, it can be observed that although the initial guess for r lies in the infeasible region in the first iteration, as shown in Fig. 5(a), the converged complete solution is successfully obtained under the proposed approach. On the other hand, although not provided here, a solution does not converge under the successive convexification process without the proposed relaxations (i.e., the generic SCP method). Thus, the results indicate that the proposed approach is less sensitive to the sub-problem infeasibility caused by a rough initial guess.

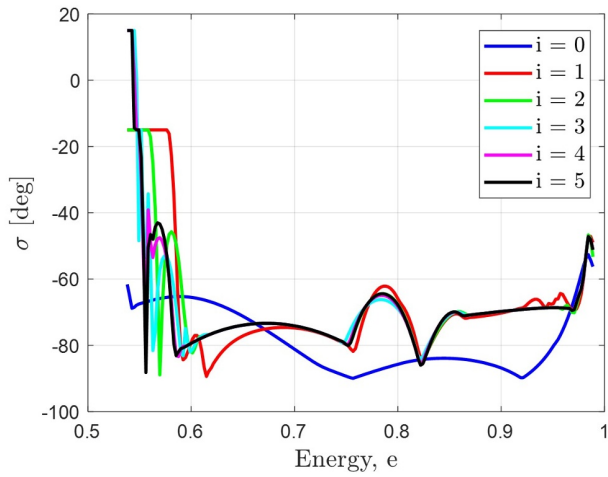
Moreover, Fig. 6 shows the convergence patterns for the performance index J and the relaxation terms v and $\delta^{(i)}$. From Fig. 6(a), we can observe that the performance index gradually decreases as the successive iterations proceed, and it successfully converges to its minimum value. As shown in Fig. 6(a), the magnitude of the relaxation term for the inequality constraint in (77) begins with a non-zero value, and the magnitude of this term approaches zero value as the number of iterations increases. It implies that the relaxation is activated in early iterations to help resolve the sub-problem infeasibility caused by a rough initial guess. Then, the relaxation effect gradually diminishes: the relaxed inequality constraint is progressively converted into the original inequality constraint. Likewise, the trust-region bound gradually decreases as the successive iterations proceed, as shown in Fig. 6(c). This feature is desirable for improving the convergence performance



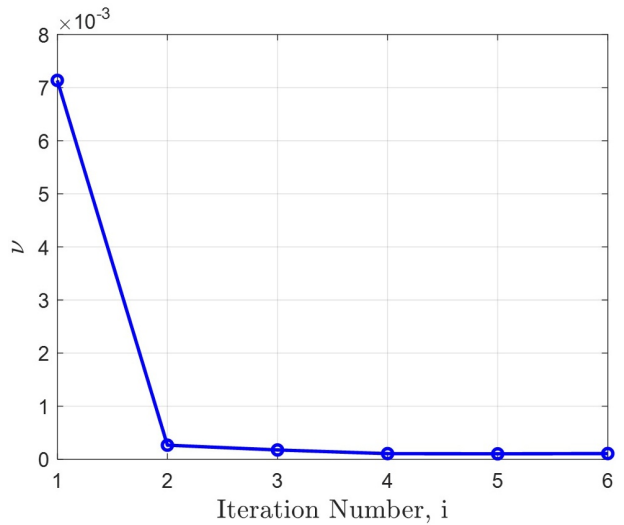
(a) Altitude vs. iteration.



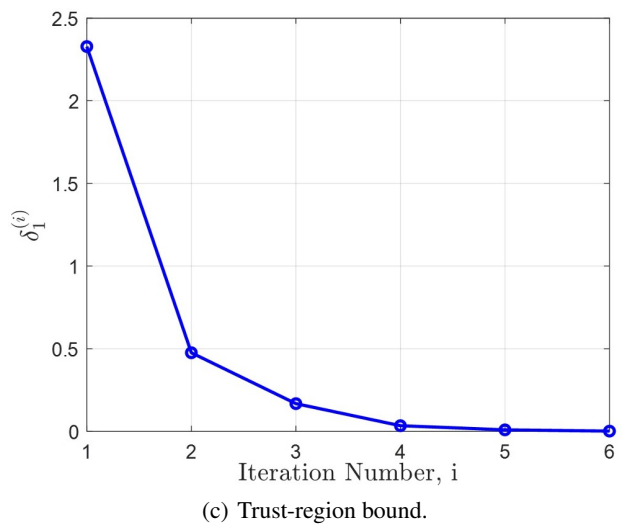
(a) Performance index J .



(b) Bank angle profile.



(b) Relaxation term for inequality constraint.



(c) Trust-region bound.

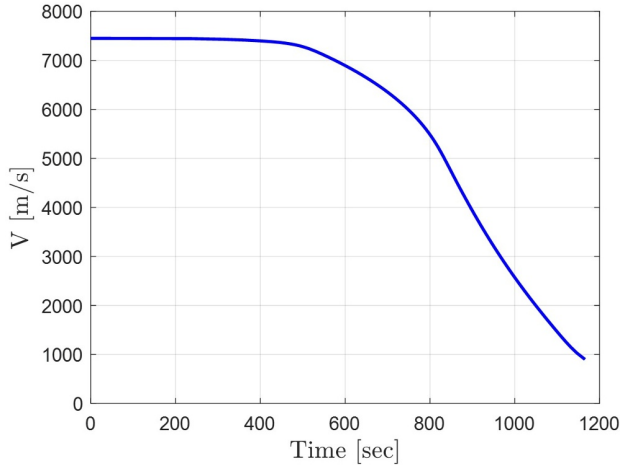
Fig. 5. Convergence patterns for altitude and bank angle profiles in successive iterations.

of the successive solution procedure.

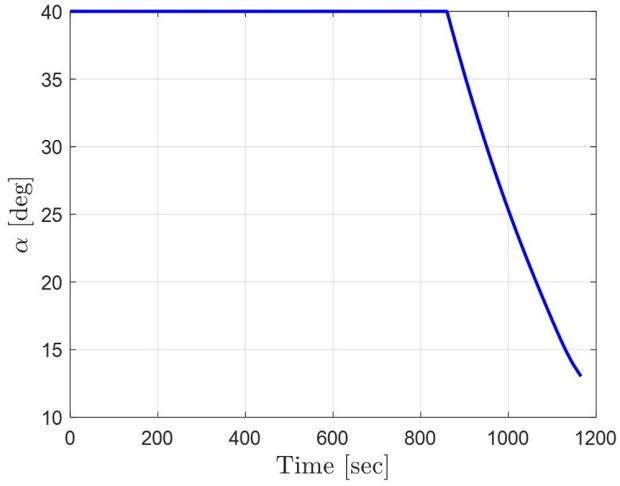
Figs. 7(a) and 7(b) represent the vehicle speed history and the corresponding angle-of-attack profile. It can be readily observed that a high angle-of-attack is maintained at the beginning of the entry trajectory for ensuring thermal protection, and the angle-of-attack gradually decreases near the final conditions for retaining trimmed flight, as in (90). Next, the converged solutions for the state variables and the control variable are plotted in Figs. 8 and 9. Fig. 8(a) and 8(b) represent the three-dimensional trajectory and the ground track history. Figs. 9(a)-9(f) depict the altitude, the latitude, the longitude, the flight path angle, the heading angle, and the bank angle, respectively. From Fig. 9, we can readily observe that all the boundary conditions for the mission, as provided in Table 1, are successfully satisfied.

Additionally, all the flight path constraints are met, as

Fig. 6. Convergence patterns for the performance index and penalty terms in successive iterations.



(a) Vehicle speed.



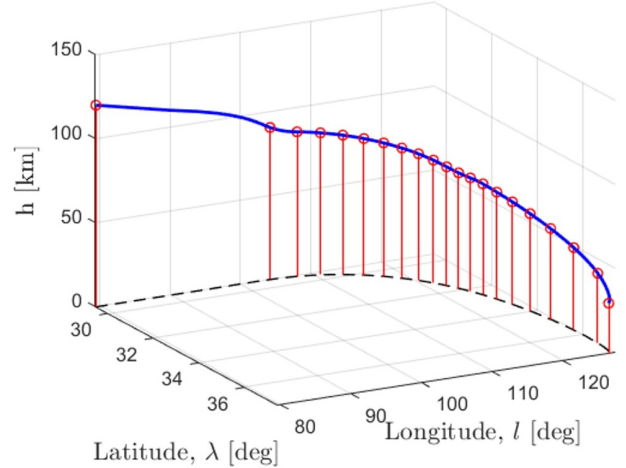
(b) Angle-of-attack.

Fig. 7. Vehicle speed and angle-of-attack profile.

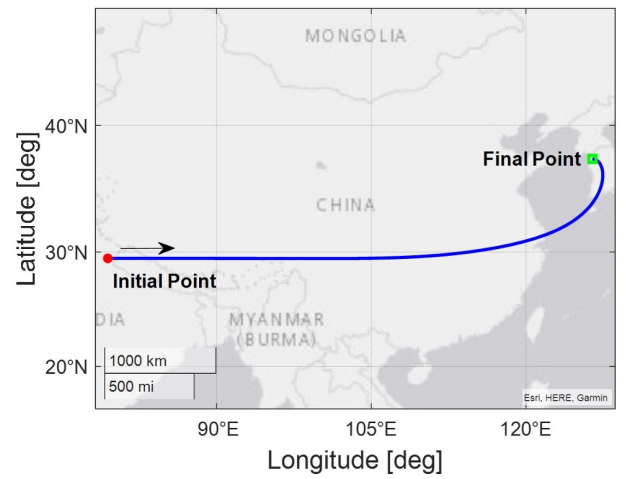
shown in Fig. 9(a). The result indicates that the satisfaction of the heat flux limit constraint is significant at the beginning of the entry guidance. In the midcourse guidance phase, the constraint for the maximum aerodynamic loading limit is activated. We can also observe that the maximum dynamic pressure constraint becomes important in the vicinity of the arrival point, as shown in Fig. 9(a). Moreover, as shown in Fig. 9(f), it can be observed that the achieved bank angle command lies within the maximum and minimum bounds on the bank angle magnitude. Finally, Fig. 10 represents the error for the kinematics constraint for the control input in (21). In this study, the relaxation error for this constraint is defined as follows:

$$\varepsilon_{\text{err}} \triangleq a_h^2 + a_v^2 - L^2. \quad (91)$$

Note that $\varepsilon_{\text{err}} = 0$ means that the kinematics constraint is satisfied in the above equation. As shown in Fig. 10, it can be readily observed that the kinematics constraint is met,



(a) 3D trajectory.



(b) Ground track.

Fig. 8. Minimum-time entry trajectory.

although the relaxation on this constraint is applied in the trajectory optimization, including the slack variable. The result obtained verifies Proposition 1.

5. CONCLUSIONS

This paper presents a way to solve the entry guidance problem by utilizing a modern convex optimization approach based on the computational guidance and control framework. The entry guidance problem is typically characterized as highly nonlinear, constrained, and nonconvex. By applying the successive convexification technique, the problem can be converted into convex sub-problems. However, the sub-problem infeasibility often occurs during the successive convexification procedure when an initial guess is rough. Additionally, high-frequency jittering is often observed in the control profile. Appropriate relaxation techniques are introduced in this study based on rigorous analysis on the issues to handle the challeng-

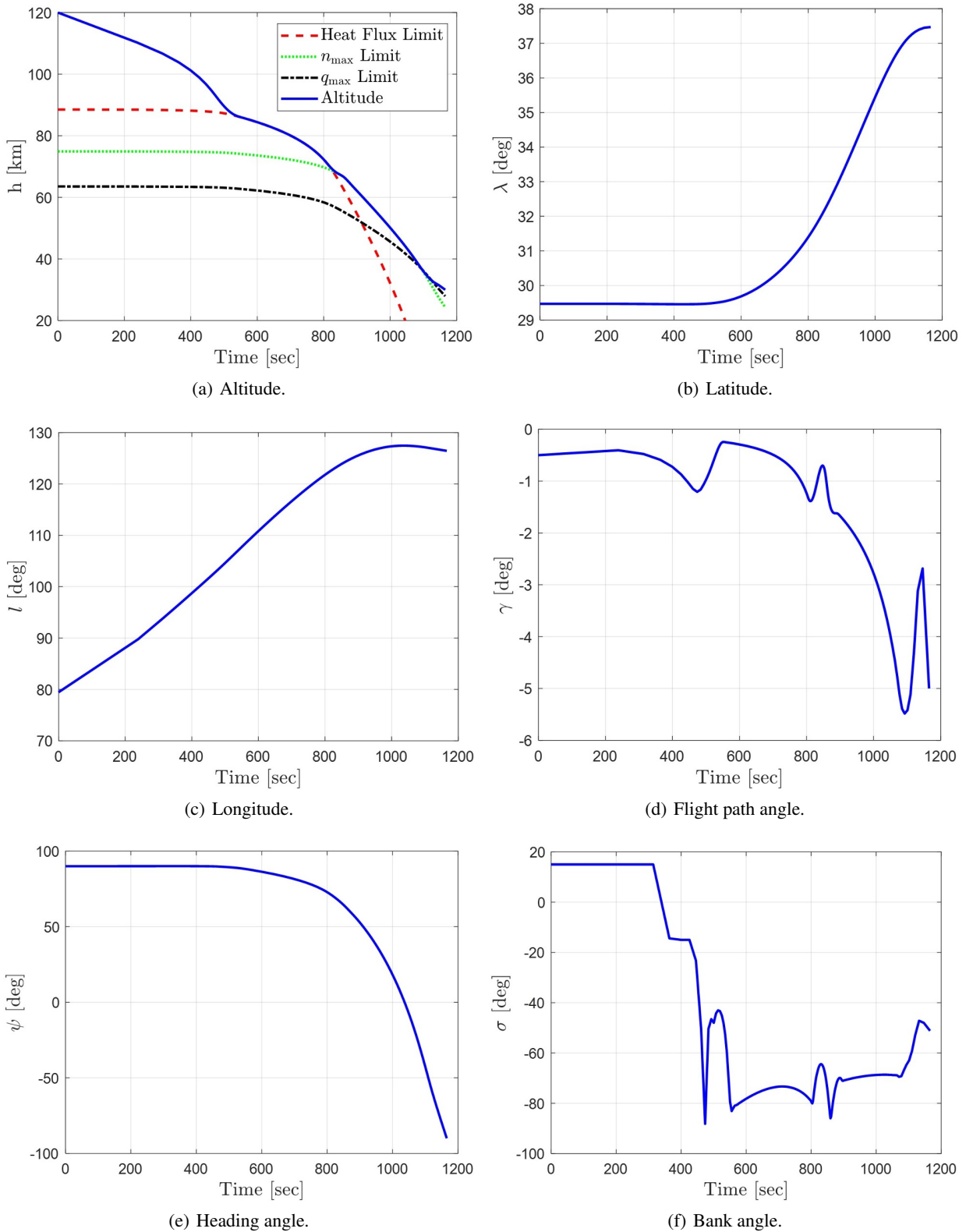


Fig. 9. State variables and control variables for minimum-time entry trajectory.

ing issues. Simulation results have shown that the proposed methods can improve the convergence characteris-

tics of the successive solution procedure in the entry guidance problem even though a rough initial guess (straight

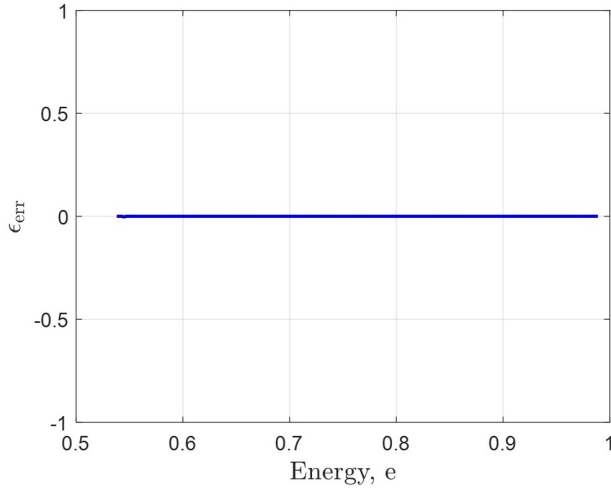


Fig. 10. The relaxation error for control input.

line approximations) is used while mitigating the high-frequency jittering issue. The solution is converged within six successive iterations, and it takes about 0.2 seconds in each iteration by utilizing a genetic solver. Thus, the proposed methods have potential in online implementation if a customized solver written an embedded program language is used.

APPENDIX A: PRELIMINARIES FOR PROOF OF PROPOSITION 1

Assumption 1: Assume that the optimal control sub-problem P_3 before discretizing has a solution. Then, as mentioned in [19], the constraints (A.9) and (A.12) are only active on a region with measure zero. i.e., exists no sub-region $[e_1, e_2] \subset [e_0, e_f]$ s.t. $a_v \stackrel{\Delta}{=} L(V^{(i)}) \cos \sigma_{\max}$ or $a_v \stackrel{\Delta}{=} L(V^{(i)}) \cos \sigma_{\min}$, or $|x - x^{(i)}| < \delta_1$ for $\forall e \in [e_1, e_2]$.

A.1. Defining equivalent problem

Based on Assumption 1, when the sub-problem P_3 is solved without discretization or continuously, the corresponding $\delta \stackrel{\Delta}{=} |x - x^{(i)}|$ and $\delta_1 = \delta_\infty$ will be determined. Therefore, for such δ_1 , we define an equivalent problem to the problem P_3 without discretization (i.e., a continuous form of problem P_3) as follows:

Minimize

$$J = c_\lambda \varepsilon_\lambda(e_f) + c_l \varepsilon_l(e_f) + \int_{e_0}^{e_f} \eta_1(x^{(i)}) r + \eta_0(x^{(i)}) + w_{v'} v(e) de \quad (\text{A.1})$$

Subject to

$$\dot{x} = F_x(x^{(i)}) x + h(x^{(i)}) u + R(x^{(i)}), \quad (\text{A.2})$$

$$r(e_0) = r_0, \lambda(e_0) = \lambda_0, l(e_0) = l_0,$$

$$\gamma(e_0) = \gamma_0, \psi(e_0) = \psi_0, \quad (\text{A.3})$$

$$r(e_f) = r_f, \gamma(e_f) = \gamma_f, \psi(e_f) = \psi_f, \quad (\text{A.4})$$

$$a_v^2 + a_h^2 \leq L(V^{(i)})^2, \quad (\text{A.5})$$

$$[\varepsilon_\lambda(e)]' = \xi_\lambda(e), \varepsilon_\lambda(e_0) = 0, \quad (\text{A.6})$$

$$[\varepsilon_l(e)]' = \xi_l(e), \varepsilon_l(e_0) = 0, \quad (\text{A.7})$$

$$|\lambda(e_f) - \lambda_f| \leq \varepsilon_\lambda(e_f), \quad |l(e_f) - l_f| \leq \varepsilon_l(e_f), \quad (\text{A.8})$$

$$L(V^{(i)}) \cos \sigma_{\max} \leq a_v \leq L(V^{(i)}) \cos \sigma_{\min}, \quad (\text{A.9})$$

$$r + v \geq g, \quad (\text{A.10})$$

$$v \geq 0, \quad (\text{A.11})$$

$$|x - x^{(i)}| \leq \delta_1, \quad (\text{A.12})$$

where $w_{v'} = w_v / \Delta e \geq 0$, $\Delta e = (e_f - e_0) / N_k$ and $g(e) \stackrel{\Delta}{=} \max\{(45), (46), (47)\}$. Additionally, ξ_λ and ξ_l are slack variables defined by derivatives of ε_λ and ε_l , respectively. Note that $x^{(i)}$ is the solution obtained from the previous i -th iteration, and it is not yet discretized. For the above optimal control problem, the state variables are $r, \lambda, l, \gamma, \psi, \varepsilon_\lambda, \varepsilon_l$, and the control variables are $a_v, a_h, v, \xi_\lambda, \xi_l$. Let F_{mn} denote the (m, n) -th component of $F_x(x^{(i)})$, and h_k denotes the k -th component of $h(x^{(i)})$.

A.2. Defining Hamiltonian and Lagrangian

In this proof, we adopt the Direct-Adjoining approach [39] to obtain the necessary conditions for the solution of the above optimal control problem. First, let us define the Hamiltonian H and the Lagrangian L as follows:

$$\begin{aligned} H \stackrel{\Delta}{=} & p_r (F_{11}r + F_{14}\gamma + h_1) \\ & + p_\lambda (F_{21}r + F_{23}l + F_{24}\gamma + F_{25}\psi + h_2) \\ & + p_l (F_{31}r + F_{34}\gamma + F_{35}\psi + h_3) \\ & + p_\gamma \left(F_{41}r + F_{44}\gamma + \frac{1}{D(V^{(i)}) (V^{(i)})^2} a_v + h_4 \right) \\ & + p_\psi \left(F_{51}r + F_{53}l + F_{54}\gamma + F_{55}\psi \right. \\ & \left. + \frac{1}{D(V^{(i)}) (V^{(i)})^2 \cos \gamma^{(i)}} a_h + h_5 \right) \\ & + p_{\varepsilon_\lambda} \xi_\lambda + p_{\varepsilon_l} \xi_l + p_0 \left(\eta_1(x^{(i)}) r \right. \\ & \left. + \eta_0(x^{(i)}) + w_{v'} v \right), \end{aligned} \quad (\text{A.13})$$

where p_0 is a non-positive constant.

$$\begin{aligned} L \stackrel{\Delta}{=} & H + \mu_u \left((L(V^{(i)}))^2 - a_v^2 - a_h^2 \right) \\ & + \mu_M \left(a_v - L(V^{(i)}) \cos \sigma_{\max} \right) \\ & + \mu_m \left(L(V^{(i)}) \cos \sigma_{\min} - a_v \right) \\ & + \mu_g (r + v - g) + \mu_v v. \end{aligned} \quad (\text{A.14})$$

Here, let us define $p \triangleq [p_r, p_\lambda, p_l, p_\gamma, p_\psi, p_{\varepsilon_\lambda}, p_{\varepsilon_l}]^T$ as the costate vector. $\mu_u, \mu_M, \mu_m, \mu_g,$ and μ_v are Lagrange Multipliers. Note that p is piecewise absolutely continuous and Lagrange multiplier functions $\mu_u, \mu_M, \mu_m, \mu_g,$ and μ_v are piecewise continuous.

A.3. Pointwise maximum condition

Assume $\{x^*, a_v^*, a_h^*, v^*, \xi_\lambda^*, \xi_l^*\}$ to be an optimal solution. The pointwise maximum condition is given by

$$\begin{aligned} & [a_v^*, a_h^*, v^*, \xi_\lambda^*, \xi_l^*]^T \\ & = \arg \max_{a_v, a_h, v, \xi_\lambda, \xi_l, \mathbf{p}, \mathbf{p}_0} H(x^*, a_v, a_h, v, \xi_\lambda, \xi_l, \mathbf{p}, \mathbf{p}_0). \end{aligned} \quad (\text{A.15})$$

A.4. Costate differential equations

By applying (4.6) from [39], we have

$$\begin{aligned} p'_r &= -F_{11}p_r - F_{21}p_\lambda - F_{31}p_l - F_{41}p_\gamma - F_{51}p_\psi \\ &\quad - p_0\eta_1(x^{(i)}) - \mu_g, \end{aligned} \quad (\text{A.16})$$

$$p'_\lambda = 0, \quad (\text{A.17})$$

$$p'_l = -F_{23}p_\lambda - F_{53}p_\psi, \quad (\text{A.18})$$

$$\begin{aligned} p'_\gamma &= -F_{14}p_r - F_{24}p_\lambda - F_{34}p_l - F_{44}p_\gamma - F_{54}p_\psi, \\ & \quad (\text{A.19}) \end{aligned}$$

$$p'_\psi = -F_{25}p_\lambda - F_{35}p_l - F_{55}p_\psi, \quad (\text{A.20})$$

$$p'_{\varepsilon_\lambda} = 0, \quad p'_{\varepsilon_l} = 0. \quad (\text{A.21})$$

A.5. Complementary slack conditions

Next, the complementary slack conditions are given by

$$\mu_u \geq 0, \quad \mu_u \left(L(V^{(i)})^2 - (a_v^*)^2 - (a_h^*)^2 \right) = 0, \quad (\text{A.22})$$

$$\mu_m \geq 0, \quad \mu_m \left(a_v^* - L(V^{(i)}) \cos \sigma_{\max} \right) = 0, \quad (\text{A.23})$$

$$\mu_M \geq 0, \quad \mu_M \left(L(V^{(i)}) \cos \sigma_{\min} - a_v^* \right) = 0, \quad (\text{A.24})$$

$$\mu_g \geq 0, \quad \mu_g (r^* + v^* - g) = 0, \quad (\text{A.25})$$

$$\mu_v \geq 0, \quad \mu_v v^* = 0. \quad (\text{A.26})$$

A.6. Transversality conditions

Since (A.8) can be rewritten as $\lambda^*(e_f) - \lambda_f + \varepsilon_\lambda^*(e_f) \geq 0$, $\lambda_f - \lambda^*(e_f) + \varepsilon_\lambda^*(e_f) \geq 0$ and $l^*(e_f) - l_f + \varepsilon_l^*(e_f) \geq 0$, $l_f - l^*(e_f) + \varepsilon_l^*(e_f) \geq 0$, we can apply the transversality conditions (4.11) from [39] as follows:

$$\mu_\lambda^+ \geq 0, \quad \mu_\lambda^+ (\lambda^*(e_f) - \lambda_f + \varepsilon_\lambda^*(e_f)) = 0, \quad (\text{A.27})$$

$$\mu_\lambda^- \geq 0, \quad \mu_\lambda^- (\lambda_f - \lambda^*(e_f) + \varepsilon_\lambda^*(e_f)) = 0, \quad (\text{A.28})$$

$$\mu_l^+ \geq 0, \quad \mu_l^+ (l^*(e_f) - l_f + \varepsilon_l^*(e_f)) = 0, \quad (\text{A.29})$$

$$\mu_l^- \geq 0, \quad \mu_l^- (l_f - l^*(e_f) + \varepsilon_l^*(e_f)) = 0. \quad (\text{A.30})$$

The conditions (4.10) from [39] would be as follows:

$$p_r(e_f^-) = \mu_r, \quad (\text{A.31})$$

$$p_\lambda(e_f^-) = \mu_\lambda^+ - \mu_\lambda^-, \quad (\text{A.32})$$

$$p_l(e_f^-) = \mu_l^+ - \mu_l^-, \quad (\text{A.33})$$

$$p_\gamma(e_f^-) = \mu_\gamma, \quad (\text{A.34})$$

$$p_\psi(e_f^-) = \mu_\psi, \quad (\text{A.35})$$

$$p_{\varepsilon_\lambda}(e_f^-) = p_0 c_\lambda + \mu_\lambda^+ + \mu_\lambda^-, \quad (\text{A.36})$$

$$p_{\varepsilon_l}(e_f^-) = p_0 c_l + \mu_l^+ + \mu_l^-, \quad (\text{A.37})$$

where $\mu_r, \mu_\gamma, \mu_\psi$ are constants.

A.7. Non-triviality condition

Additionally, the non-triviality condition is given by

$$\begin{aligned} & (\mu_u, \mu_m, \mu_M, \mu_g, \mu_v, \mu_\lambda^+, \mu_\lambda^-, \mu_l^+, \mu_l^-, \mu_\gamma, \\ & \mu_\psi, \mathbf{p}, \mathbf{p}_0) \neq 0, \quad \text{for } \forall e \in [e_0, e_f]. \end{aligned} \quad (\text{A.38})$$

Until now, the conditions (4.4) and (4.6) to (4.11) from [39] are applied. Hereafter, applying (4.5) will take an essential role in the following proof.

APPENDIX B: PROOF OF PROPOSITION 1

Based on the preliminaries described in the previous appendix, Proposition 1 will be proven hereafter. By adopting the similar approach used in [19], first assume $(a_v^*)^2 + (a_h^*)^2 < L(V^{(i)})^2$ is uniform on $[e_0, e_f]$. Then, (A.22) leads to $\mu_u = 0$. In this context, $f(e) = 0$ for some function f on $[e_0, e_f]$ means that $f(e) = 0$ almost everywhere on $[e_0, e_f]$.

Now from the assumption that $a_v = L(V^{(i)}) \cos \sigma_{\max}$ and $a_v = L(V^{(i)}) \cos \sigma_{\min}$ are not satisfied almost everywhere, by (A.23) and (A.24), we conclude that $\mu_m = 0$ and $\mu_M = 0$.

From (A.15), H is maximized over ξ_λ and ξ_l . Additionally, since these are unbounded, $p_{\varepsilon_\lambda} = 0$ and $p_{\varepsilon_l} = 0$ are required for maximizing H to exist. Then applying (4.5) from [39], $\partial_{a_v} L = \partial_{a_h} L = \partial_v L = 0$ as

$$\begin{aligned} \partial_{a_v} L &= \frac{1}{D(V^{(i)}) (V^{(i)})^2} p_\gamma - 2\mu_u a_v - \mu_m + \mu_M \\ &= \frac{1}{D(V^{(i)}) (V^{(i)})^2} p_\gamma = 0, \quad \therefore p_\gamma = 0. \end{aligned} \quad (\text{B.1})$$

$$\begin{aligned} \partial_{a_h} L &= \frac{1}{D(V^{(i)}) (V^{(i)})^2 \cos \gamma^{(i)}} p_\psi - 2\mu_u a_h \\ &= \frac{1}{D(V^{(i)}) (V^{(i)})^2 \cos \gamma^{(i)}} p_\psi = 0, \quad \therefore p_\psi = 0. \end{aligned} \quad (\text{B.2})$$

$$\partial_v L = p_0 w_{v'} + \mu_g + \mu_v = 0. \quad (\text{B.3})$$

Here, (B.2) implies $p'_\psi = 0$. Then substituting the result from (B.2) to (A.18) and (A.20), we can obtain

$$p'_l = -F_{23}p_\lambda, \quad (\text{B.4})$$

$$p'_\psi = -F_{25}p_\lambda - F_{35}p_l = 0. \quad (\text{B.5})$$

Then, since $p_l = -(F_{25}/F_{35})p_\lambda$, differentiating both sides by e gives

$$\begin{aligned} p'_l &= -(F_{25}/F_{35})p'_\lambda - (F_{25}/F_{35})'p_\lambda \\ &= -(F_{25}/F_{35})'p_\lambda = -F_{23}p_\lambda. \end{aligned} \quad (\text{B.6})$$

Because $p'_\lambda = 0$. From this condition, we have

$$\left(F_{23} - \left(\frac{F_{25}}{F_{35}} \right)' \right) p_\lambda = 0. \quad (\text{B.7})$$

By explicitly substituting each component of $F_x(x^{(i)})$, one can quickly check that $F_{23} - (F_{25}/F_{35})' \neq 0$, hence $p_\lambda = 0$ and $p_l = 0$ from (B.5). From the preceding results with (A.32) and (A.33), $\mu_\lambda^+ = \mu_\lambda^-$ and $\mu_l^+ = \mu_l^-$.

Given that p_{ε_λ} is piecewise absolutely continuous on $[e_0, e_f]$, $\exists \varepsilon > 0$ s.t. p_{ε_λ} is absolutely continuous on $(e_f - \varepsilon, e_f)$. With the fact that $p_{\varepsilon_\lambda} = 0$ almost everywhere, this implies that $p_{\varepsilon_\lambda}(e) = 0$ is uniform on $(e_f - \varepsilon, e_f)$, hence $p_{\varepsilon_\lambda}(e_f^-) = 0$.

Now from (A.36), we have

$$p_{\varepsilon_\lambda}(e_f^-) = p_0c_\lambda + \mu_\lambda^+ + \mu_\lambda^- = 0. \quad (\text{B.8})$$

Since it is evident that the inequalities from (A.8) must be tight in order to achieve minimum cost, either $\lambda^*(e_f) - \lambda_f + \varepsilon_\lambda^*(e_f) = 0$ or $\lambda_f - \lambda^*(e_f) + \varepsilon_\lambda^*(e_f) = 0$. First, suppose that only one of the two is zero and the other to be non-zero. Then, (A.27) and (A.28) provide that at least one of μ_λ^+ and μ_λ^- is 0. Then, $\mu_\lambda^+ = \mu_\lambda^-$ implies that both $\mu_\lambda^+ = \mu_\lambda^- = 0$. An analogous approach to l instead of λ proves that $\mu_l^+ = \mu_l^- = 0$. Then, (B.8) directly shows that $p_0 = 0$. Since it is proven that all the other terms on the right-hand side (RHS) of (A.16) except μ_g are zero, $p_r = 0$ implies $\mu_g = 0$. Then, (B.3) directly proves that $\mu_v = 0$.

Now when both, $\lambda^*(e_f) - \lambda_f + \varepsilon_\lambda^*(e_f) = 0$ and $\lambda_f - \lambda^*(e_f) + \varepsilon_\lambda^*(e_f) = 0$, this is simply when the final state $\lambda^*(e_f) = \lambda_f$ and $\varepsilon_\lambda^*(e_f) = 0$. Then, since all the costate vectors are proven to be zero, (A.16) becomes

$$-p_0\eta_1(x^{(i)}) - \mu_g = 0. \quad (\text{B.9})$$

With (B.3), eliminating p_0 gives

$$\left(\eta_1(x^{(i)}) - w'_v \right) \mu_g + \eta_1(x^{(i)}) \mu_v = 0. \quad (\text{B.10})$$

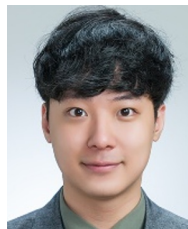
Since both μ_g and μ_v are non-negative values, we can conclude that $\mu_g = \mu_v = 0$ under the mild assumption $\eta_1(x^{(i)}) - w'_v > 0$. Substituting the results to (B.3) again, we have $p_0 = 0$ and given $\mu_\lambda^+, \mu_\lambda^-, \mu_l^+, \mu_l^- \geq 0$, it is direct-forward from (A.36) and (A.37) that $\mu_\lambda^+ = \mu_\lambda^- = \mu_l^+ = \mu_l^- = 0$. Lastly, (A.31), (A.34), and (A.35) imply $\mu_r = \mu_\psi = 0$.

Hence assuming that convex relaxation is violated leads to contradiction on non-triviality condition.

REFERENCES

- [1] K. Hu, F. Chen, and Z. Cheng, "Fuzzy adaptive hybrid compensation for compound faults of hypersonic flight vehicle," *International Journal of Control, Automation, and Systems*, vol. 19, no. 6, pp. 2269-2283, 2021.
- [2] B. W. Chen and L. G. Tan, "Adaptive anti-saturation tracking control with prescribed performance for hypersonic vehicle," *International Journal of Control, Automation, and Systems*, vol. 18, no. 2, pp. 394-404, 2020.
- [3] P. Li, P. Huang, C. Y. He, and X. Q. Liu, "Finite-time dynamic surface fault-tolerant control for hypersonic vehicle with mismatched disturbances," *International Journal of Control, Automation, and Systems*, vol. 19, no. 7, pp. 2309-2322, 2021.
- [4] J. Harpold and C. Graves Jr, *Shuttle Entry Guidance*, American Astronautical Society, 1978.
- [5] J. C. Harpold and D. E. Gavert, "Space shuttle entry guidance performance results," *Journal of Guidance, Control, and Dynamics*, vol. 6, no. 6, pp. 442-447, 1983.
- [6] A. J. Roenneke and A. Markl, "Re-entry control to a drags-energy profile," *Journal of Guidance, Control, and Dynamics*, vol. 17, no. 5, pp. 916-920, 1994.
- [7] K. D. Mease and J. P. Kremer, "Shuttle entry guidance revisited using nonlinear geometric methods," *Journal of Guidance, Control, and Dynamics*, vol. 17, no. 6, pp. 1350-1356, 1994.
- [8] P. Lu, "Entry guidance and trajectory control for reusable launch vehicle," *Journal of Guidance, Control, and Dynamics*, vol. 20, no. 1, pp. 143-149, 1997.
- [9] P. Lu, "Predictor-corrector entry guidance for low-lifting vehicles," *Journal of Guidance, Control, and Dynamics*, vol. 31, no. 4, pp.1067-1075, 2008.
- [10] Z. Shen and P. Lu, "Onboard generation of three-dimensional constrained entry trajectories," *Journal of Guidance, Control, and Dynamics*, vol. 26, no. 1, pp. 111-121, 2003.
- [11] S. Xue and P. Lu, "Constrained predictor-corrector entry guidance," *Journal of Guidance, Control, and Dynamics*, vol. 33, no. 4, pp.1273-1281, 2010.
- [12] P. Lu, "Entry guidance: A unified method," *Journal of Guidance, Control, and Dynamics*, vol. 37, no. 3, pp. 713-728, 2014.
- [13] P. Lu, "Introducing computational guidance and control," *Journal of Guidance, Control, and Dynamics*, vol. 40, no. 2, p. 193, 2017.
- [14] T. H. Kim, J. Park, and J. H. Kim, "Computational issues in sparse and dense formulations of integrated guidance and control with constraints," *International Journal of Aeronautical and Space Sciences*, vol. 21, no. 3, pp. 826-835, 2020.
- [15] Q. Zhang, Z. Gong, Z. Yang, and Z. Chen, "Distributed convex optimization for flocking of nonlinear multi-agent systems," *International Journal of Control, Automation, and Systems*, vol. 17, no. 5, pp. 1177-1183, 2019.

- [16] X. Ping, S. Yang, B. Ding, T. Raissi, and Z. Li, "A convexity approach to dynamic output feedback robust MPC for LPV systems with bounded disturbances," *International Journal of Control, Automation, and Systems*, vol. 18, no. 6, pp. 1378-1391, 2020.
- [17] D. F. Zhang, S. P. Zhang, Z. Q. Wang, and B. C. Lu, "Dynamic control allocation algorithm for a class of distributed control systems," *International Journal of Control, Automation, and Systems*, vol. 18, no. 2, pp. 259-270, 2020.
- [18] H. H. Kwon and H. L. Choi, "A convex programming approach to mid-course trajectory optimization for air-to-ground missiles," *International Journal of Aeronautical and Space Sciences*, vol. 21, no. 2, pp. 479-492, 2020.
- [19] X. Liu, Z. Shen, and P. Lu, "Entry trajectory optimization by second-order cone programming," *Journal of Guidance, Control, and Dynamics*, vol. 39, no. 2, pp. 227-241, 2016.
- [20] X. Liu, P. Lu, and B. Pan, "Survey of convex optimization for aerospace applications," *Astrodynamics*, vol. 1, no. 1, pp. 23-40, 2017.
- [21] Y. Yang and B. Ding, "An iterative optimization approach for fuzzy predictive control," *International Journal of Control, Automation, and Systems*, vol. 18, no. 8, pp. 2157-2164, 2020.
- [22] Z. Wang and M. J. Grant, "Constrained trajectory optimization for planetary entry via sequential convex programming," *Journal of Guidance, Control, and Dynamics*, vol. 40, no. 10, pp. 2603-2615, 2017.
- [23] Z. Wang and M. J. Grant, "Autonomous entry guidance for hypersonic vehicles by convex optimization," *Journal of Spacecraft and Rockets*, vol. 55, no. 4, pp. 993-1006, 2018.
- [24] J. Wang, N. Cui, and C. Wei, "Rapid trajectory optimization for hypersonic entry using a pseudospectral-convex algorithm," *Proceedings of the Institution of Mechanical Engineers, Part G: Journal of Aerospace Engineering*, vol. 233, no. 14, pp. 5227-5238, 2019.
- [25] Z. Wang and Y. Lu, "Improved sequential convex programming algorithms for entry trajectory optimization," *Journal of Spacecraft and Rockets*, vol. 57, no. 6, pp. 1373-1386, 2020.
- [26] H. Han, D. Qiao, H. Chen, and X. Li, "Rapid planning for aerocapture trajectory via convex optimization," *Aerospace Science and Technology*, vol. 84, pp. 763-775, 2019.
- [27] D. J. Zhao and Z. Y. Song, "Reentry trajectory optimization with waypoint and no-fly zone constraints using multiphase convex programming," *Acta Astronautica*, vol. 137, pp. 60-69, 2017.
- [28] L. Blackmore, "Autonomous precision landing of space rockets," *Frontiers of Engineering: Reports on Leading-Edge Engineering from the 2016 Symposium*, vol. 46, pp. 15-20, 2016.
- [29] M. Szmuk and B. Acikmese, "Successive convexification for 6-DOF mars rocket powered landing with free-final-time," *Proc. of AIAA Guidance, Navigation, and Control Conference*, p. 0617, 2018.
- [30] H. Roh, Y. J. Oh, M. J. Tahk, K. J. Kwon, and H. H. Kwon, "L1 penalized sequential convex programming for fast trajectory optimization: With application to optimal missile guidance," *International Journal of Aeronautical and Space Sciences*, vol. 21, no. 4, pp. 493-503, 2020.
- [31] R. Fletcher, "A penalty method for nonlinear constraints," *Numerical Optimization 1984*, SIAM Publications, pp. 26-40, 1985.
- [32] P. J. Shaffer, "Optimal trajectory reconfiguration and retargeting for the X-33 reusable launch vehicle," *Naval Postgraduate School Monterey CA*, Tech. Rep., 2004.
- [33] P. J. Shaffer, I. M. Ross, M. W. Oppenheimer, D. B. Doman, and K. P. Bollino, "Fault-tolerant optimal trajectory generation for reusable launch vehicles," *Journal of Guidance, Control, and Dynamics*, vol. 30, no. 6, pp. 1794-1802, 2007.
- [34] N. X. Vinh, "Optimal trajectories in atmospheric flight," *Space Mankind's Fourth Environment*, pp. 449-468, 1982.
- [35] X. Liu, Z. Shen, and P. Lu, "Exact convex relaxation for optimal flight of aerodynamically controlled missiles," *IEEE Transactions on Aerospace and Electronic Systems*, vol. 52, no. 4, pp. 1881-1892, 2016.
- [36] J. H. Chae, T. K. Mankodi, S. M. Choi, and R. S. Myong, "Combined effects of thermal non-equilibrium and chemical reactions on hypersonic air flows around an orbital reentry vehicle," *International Journal of Aeronautical and Space Sciences*, vol. 21, no. 3, pp. 612-626, 2020.
- [37] X. Liu, Z. Shen, and P. Lu, "Closed-loop optimization of guidance gain for constrained impact," *Journal of Guidance, Control, and Dynamics*, vol. 40, no. 2, pp. 453-460, 2016.
- [38] M. ApS, "MOSEK optimization toolbox for MATLAB," *User's Guide and Reference Manual*, version, vol. 4, 2019.
- [39] R. F. Hartl, S. P. Sethi, and R. G. Vickson, "A survey of the maximum principles for optimal control problems with state constraints," *SIAM Review*, vol. 37, no. 2, pp. 181-218, 1995.



Juho Bae is currently working on a B.S. degree in electrical engineering and mathematics from Korea Advanced Institute of Science and Technology (KAIST), Daejeon, Korea. His research interests include adaptive control, entry guidance, numerical optimization, and convex programming.



Sang-Don Lee received his B.S. degree in mechanical engineering from Hanyang University, Seoul, Korea, in 2019, and an M.S. degree in aerospace engineering from Korea Advanced Institute of Science and Technology (KAIST), Daejeon, Korea, in 2021. He is currently a Ph.D. student in the Department of Aerospace Engineering from KAIST, Daejeon, Korea. His research interests include trajectory optimization, convex programming, and reinforcement learning.



Young-Won Kim received his B.S. degree in mechanical engineering from Handong University in 2014, and an M.S. degree in aerospace engineering from Korea Advanced Institute of Science and Technology (KAIST), in 2016, respectively. Currently, he is a Ph.D. candidate in aerospace engineering from KAIST, Daejeon, Korea. His area of scientific interest includes advanced missile guidance and control, and robust control of Personal Air Vehicle (PAV).



Chang-Hun Lee received his B.S., M.S., and Ph.D. degrees in aerospace engineering from Korea Advanced Institute of Science and Technology (KAIST), in 2008, 2010, and 2013, respectively. From 2013 to 2015, he was a Senior Researcher for Guidance and Control Team, Agency for Defense Development, Daejeon, Korea. From 2016 to 2018, he was a Research

Fellow for School of Aerospace, Transportation, and Manufacturing, Cranfield University, Bedford, United Kingdom. Since 2019, he has been with the Department of Aerospace Engineering, KAIST, Daejeon, Korea, where he is currently an Associate Professor. His recent research interests include advanced missile guidance and control, cooperative control for unmanned aerial vehicles, target tracking filter, deep learning, and aviation data analytics. Currently, he is a technical editor of International Journal of Aeronautical and Space Science.



Sung-Yug Kim received his B.S. degrees in naval architecture and ocean engineering from Inha University in 1987, Incheon, Korea. He served as a navy Lieutenant from 1987 to 1994. He was a Senior Researcher with the Korea Aerospace Industries, Ltd., Changwon, from 1994 to 2000. He has been a Principal Researcher with the Unmanned Aircraft System Research Division, Korea Aerospace Research Institute (KARI) since 2001. His research interests include system integration and hardware design. He has been involved in projects developing UAVs, especially in the design and implementation of hardware for flight dynamics and control.

Publisher's Note Springer Nature remains neutral with regard to jurisdictional claims in published maps and institutional affiliations.